



HAL
open science

Fabrication of Hyperuniform Dielectric Networks via Heat-Induced Shrinkage Reveals a Bandgap at Telecom Wavelengths

Stefan Aeby, Geoffroy Aubry, Luis Froufe-Pérez, Frank Scheffold

► **To cite this version:**

Stefan Aeby, Geoffroy Aubry, Luis Froufe-Pérez, Frank Scheffold. Fabrication of Hyperuniform Dielectric Networks via Heat-Induced Shrinkage Reveals a Bandgap at Telecom Wavelengths. *Advanced Optical Materials*, In press, pp.2200232. 10.1002/adom.202200232 . hal-03714023

HAL Id: hal-03714023

<https://hal.science/hal-03714023>

Submitted on 6 Oct 2022

HAL is a multi-disciplinary open access archive for the deposit and dissemination of scientific research documents, whether they are published or not. The documents may come from teaching and research institutions in France or abroad, or from public or private research centers.

L'archive ouverte pluridisciplinaire **HAL**, est destinée au dépôt et à la diffusion de documents scientifiques de niveau recherche, publiés ou non, émanant des établissements d'enseignement et de recherche français ou étrangers, des laboratoires publics ou privés.



Distributed under a Creative Commons Attribution 4.0 International License

Fabrication of Hyperuniform Dielectric Networks via Heat-Induced Shrinkage Reveals a Bandgap at Telecom Wavelengths

Stefan Aeby,* Geoffroy J. Aubry, Luis S. Froufe-Pérez, and Frank Scheffold*

Recent studies report photonic bandgaps (PBGs) in disordered hyperuniform network structures numerically and experimentally for high enough refractive index contrast. However, the smallest experimental central gap wavelength that one can realize experimentally is not close to the essential near-infrared light spectrum with adverse consequences for specific applications and more advanced experimental studies. Indeed, standard direct laser writing (DLW) lithography does not allow fabrication at a much higher resolution. Here, the authors demonstrate heat-treatment induced uniform shrinkage of the network's polymer template obtained by DLW to reach smaller feature sizes and subsequent silicon coating, resulting in a pronounced gap near telecom wavelengths.

1. Introduction

Amorphous and crystalline dielectric networks with tetrahedral vertices, including diamond structures, are widely considered champion photonic materials.^[1,2] Such materials open complete photonic bandgaps (PBGs) in 3D at refractive indices between two and three (in air). The bandgap width becomes substantial if the dielectric material is silicon ($n \approx 3.5$) or another high index material. There seems to be consensus in the recent literature that the superior photonic properties stem from combining the tetrahedral local topology—the same for all vertices—the moderate filling fraction between 20–40%, short-range structural correlations, and long-range uniformity. Different structural designs are possible, such as (stealthy) hyperuniformity, local self-uniform,^[3] crystalline

and amorphous diamond networks,^[2,4] foam-based heterostructures,^[5,6] and more. These all lead to excellent photonic properties, and it seems that slightly different designs lead to comparable outcomes. A final verdict on which might be the optimal design is still outstanding. Crystals usually perform better concerning the opening of a complete bandgap,^[7] but amorphous structures offer advantages for designing free-form waveguides and for non-iridescent structural colors.^[8–13] Many recently proposed photonic network materials are computer-designed, and efficient self-assembly processes are either missing or in their infancy. Photonic

bandgap materials fabricated via self-assembly are still rare,^[14] although recently, the research community reported substantial progress in this direction.^[4] Consequently, most of the literature on the dielectric photonic network's optical properties either reports numerical simulation results or experimental data on structures fabricated with lithographic techniques. Direct laser writing (DLW) lithography is the most used technique to fabricate 3D polymer templates for subsequent conversion into higher index materials such as silicon or titanium dioxide.^[15–19]

In 2009, the seminal work of Florescu et al.,^[20] established general design rules for amorphous PBG materials. The authors showed that disordered hyperuniform dielectric media in 2D can exhibit an isotropic complete PBG—nearly as wide as the corresponding crystal structure.^[21] The 2D results were later extended to 3D materials using the same design principles.^[22,23] Both 2D and 3D photonic materials can open a full bandgap.^[20,22–24] Amorphous dielectrics also show Anderson localization of light near the gap, but the behavior is qualitatively different in 3D compared to 2D.^[23,25,26] A detailed discussion about the concept of hyperuniformity can be found in ref. [27]. Briefly, hyperuniformity measures uniformity on larger length scales and encodes a particular kind of “hidden structural order” even for globally disordered structures. In reciprocal space, with a scattering vector modulus $q = |\vec{q}|$, hyperuniformity corresponds to a vanishing low- q structure factor $S(q \rightarrow 0) \rightarrow 0$, which implies the absence of density fluctuations on large length scales. “Stealthy” hyperuniformity means that there is a sharp cut-off $S(q < q_c) \equiv 0$.^[27,28] The hyperuniformity concept has recently drawn much attention for photonic materials and other domains of condensed matter physics and biology.^[27] For disordered hyperuniform networks, the gap-wavelength is set by the characteristic length

S. Aeby, G. J. Aubry, L. S. Froufe-Pérez, F. Scheffold
Department of Physics
University of Fribourg
Fribourg 1700, Switzerland
E-mail: stefan.aeby@unifr.ch; frank.scheffold@unifr.ch

G. J. Aubry
Université Côte d'Azur
CNRS, Institut de Physique de Nice (INPHYNI)
Nice 06100, France

 The ORCID identification number(s) for the author(s) of this article can be found under <https://doi.org/10.1002/adom.202200232>.

© 2022 The Authors. Advanced Optical Materials published by Wiley-VCH GmbH. This is an open access article under the terms of the Creative Commons Attribution License, which permits use, distribution and reproduction in any medium, provided the original work is properly cited.

DOI: 10.1002/adom.202200232

scale of short-range spatial correlations, quantified by the first peak of the real-space density autocorrelation function a .^[24] For a silicon volume filling fraction of 20%, Liew et al., report $\lambda_{\text{Gap}} \approx 1.7a$ for the mid-gap wavelength.^[22] The DLW-fabrication of amorphous (hyperuniform) dielectric 3D networks is more challenging than, for example, fabricating woodpile photonic crystals.^[15] The lithographic resolution of conventional DLW is limited to about 150–200 nm laterally and 400–550 nm axially. The smallest gap wavelength reported so far for hyperuniform networks was $\lambda_{\text{Gap}} \approx 2.4 \mu\text{m}$, after converting the template into silicon.^[19] For the desired near-infrared (NIR) gap-wavelength of $\lambda_{\text{Gap}} = 1.5 - 1.7 \mu\text{m}$, $a \lesssim 1 \mu\text{m}$ and thus the length of the connecting rods $d \ll a$ would become smaller than the DLW axial resolution. Compared to woodpile crystals where all the rods lie parallel to the surface plane, the orientation of rods is random in a hyperuniform disordered network. We can thus not benefit from the superior lateral resolution in DLW. Consequently, standard DLW-fabrication is unsuitable for fabricating photonic networks with bandgaps near telecom wavelengths, representing a significant hurdle for introducing (hyperuniform) dielectric networks into practical applications. It also hinders the more precise optical characterization using familiar visible and NIR wavelength laser sources, advanced digital cameras, and single-photon detectors.^[29–32]

Using beam shaping and stimulated emission depletion (STED)-inspired lithography, Fischer et al.^[33] have reported $\approx 2.3 \times$ improved resolution compared to standard DLW. However, these more exploratory DLW-techniques are not readily available and require sophisticated instrumentation and optimization of the lithographic process. It is currently unknown whether one can routinely realize the reported resolution improvement for the hyperuniform networks discussed here. Alternatively, Liu et al.,^[34] recently reported a fivefold resolution improvement based on a thermal processing and shrinking approach applied to woodpile photonic crystals. One can realize the latter without changes to the standard commercially available DLW-lithography, which provides a more straightforward way to reach a higher fabrication resolution. One could also combine both methods and possibly exploit the cumulative improvement in resolution, which has not been attempted so far. Here, we present an implementation of the shrinking approach to 3D-hyperuniform dielectric networks using stress releasing support structures, critical point drying (CPD), and post-processing of the forms by a high-temperature thermal treatment. Shrinking fragile networks while keeping access to the systems from both sides unobstructed poses several additional problems and challenges we managed to overcome. We demonstrate uniform shrinkage by a factor of two and thus obtain stealthy hyperuniform photonic network structures with unprecedented gap wavelengths, down to telecom wavelengths, by infiltrating the shrunken template with a higher index material.

2. Results

2.1. Fabrication

We use the commercial DLW platform Photonics Professional (Nanoscribe GmbH, Germany) to write polymer templates of

networks. As a seed pattern, we use a stealthy hyperuniform point pattern generated numerically (stealthiness parameter $\chi = 0.65$).^[24,27] Next, we perform a Delaunay tessellation on the seed pattern. The tessellation divides the design into tetrahedrons, and the tetrahedrons' mass centers are connected with dielectric rods, creating the desired tetravalent network structure in silico. The computer-generated 3D structure, outer dimensions $70 \times 70 \times 23 \mu\text{m}^3$, is then fed into the DLW-software and reproduced as a polymer cast using an optimized writing algorithm developed in-house.^[35]

One critical issue that occurs when developing the structure is non-uniform shrinking. Attached to the substrate on one face, uneven contraction and deformation forces act on the polymer.^[36] One can solve this problem by placing the structure on a sacrificial supporting grid that can deform, release stress, and keep the form intact. However, in the previous work, the supporting grid covered the whole surface underneath the sample,^[34,37] which is not suitable in our case since it would obstruct the incident light path in optical transmission measurements. Also, reaching our goal of reducing the fragile network's length scales by 50% (by thermal shrinkage) would be challenging with the type of rigid supporting grid used in earlier studies.^[37] Therefore, while we retain the idea of the sacrificial supporting structure, we have to adapt it. The grid has to remain flexible and grant unobstructed optical access to the sample. The challenge is that the grid must remain rigid enough to prevent unwanted movement during the writing process. We tested different architectures and configurations and found, by trial and error, that a spider-leg-like support structure is suitable to reach the contemplated goals. **Figure 1** shows an illustration of the hyperuniform network (in blue). The footprint of the supporting grid is a ring whose inner diameter is larger than the network's footprint. Cross-rods connect neighboring legs to increase stability during the writing process. Every portion connects to an outer rod of the hyperuniform network, which explains the uneven spacing between the spider legs. We use the direct laser writing instrument to print the support structure and the network based on its digital representation, finely tuning the experimental parameters such as writing protocol, speed, and exposure of the photoresist (IP-Dip, Nanoscribe, Germany). After the writing process is complete, we develop the structures for 5 min and replace the developer once. We rinse the sample with isopropanol, the solvent we subsequently use in CPD. While undergoing this procedure and CPD, no capillary forces act on the structure, resulting in undeformed systems. Tests without CPD often resulted in collapsed and deformed structures. Still, during development and CPD, the samples shrink by about 10%, as is commonly observed in DLW-studies.^[35,38]

Next, we place the polymeric structures in a temperature-controlled heating stage (Linkam Scientific Instruments Ltd FTIR600). The chamber is constantly flooded with nitrogen to prevent the oxidation of the polymer. We raise the heating stage temperature from room temperature to $T = 450 \text{ }^\circ\text{C}$ at a rate of $10 \text{ }^\circ\text{C}$ per minute. Below a set temperature of $T = 430 \text{ }^\circ\text{C}$ we observe no shrinkage; see also Supporting Information in ref. [39]. We then kept the sample at the highest temperature for 4–10 min, depending on the desired shrinking ratio. Finally, the chamber is cooled using a water chiller. We

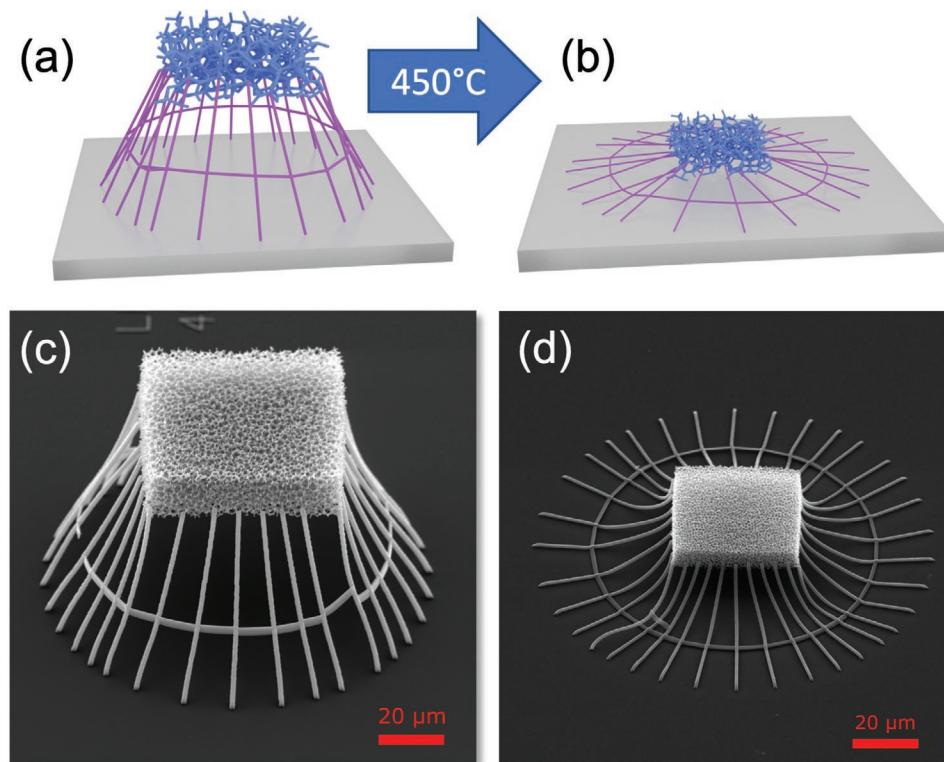


Figure 1. Digital rendering of a hyperuniform polymer network positioned on supporting “spider”-legs. The hyperuniform network itself is shown in blue color, the supporting structure in magenta color. a) Before shrinking, the structure is held high above the substrate. b) During the heat treatment, the network shrinks uniformly, and the legs partly collapse until, eventually, the network almost touches the substrate. Panels (c) and (d) show a typical scanning electron microscope (SEM) images of hyperuniform polymer networks before ($60.6 \times 60.6 \times 19.5 \mu\text{m}^3$) and after the heat treatment ($38.3 \times 38.3 \times 12.2 \mu\text{m}^3$).

found that heat treatment for more than 10 min led to damage to the structure.

Before the heat treatment, the footprint of the sample is $\approx 60 \times 60 \mu\text{m}^2$ with a thickness $L = 20 \mu\text{m}$ (Figure 3c). After the heat treatment, we find isotropically shrunken forms with preserved structural integrity. The measured edge lengths are between 30–40 μm , reduced by almost a factor of two (Figure 1d). Distances between the substrate and the network structure are also reduced, but they never touch (Figure 1d).

2.2. Scattering Properties of the Polymer Template

We assess the bulk properties of the polymer templates by performing small-angle light scattering experiments. To this end, we collect experimental data using an in-house built small-angle light scattering setup, Figure 2a. A helium–neon laser ($\lambda = 632.8 \text{ nm}$) passes through a diaphragm and is then focused on the sample using a lens ($f = 35 \text{ mm}$). The incident beam passes through the glass substrate. We nearly match the refractive index of the dielectric network ($n = 1.52$) by applying a drop of decaline ($n = 1.481$) on top of the sample. The drop curvature reduces the refraction of scattered light at the droplet/air interface, and in the following, we neglect refraction. We collect scattered light on a thin white plastic screen at a distance of $z = 14 \text{ cm}$. Using a digital camera,

we take a back-side image of the screen, Figure 2b. We compute the radial average of the scattered intensity, and by measuring the radial distance u from the center, we calculate the scattering angle θ via the relation $\tan \theta = u/z$.^[35]

The recorded data is significantly affected by stray light and diffraction from the entire sample. The latter is difficult to suppress due to the small sample size. Focusing the incident laser beam too much makes the beam divergent, while focusing too little leads to more diffraction and stray light. As shown in Figure 2b, we partly suppress such contamination by masking stray light and the sample’s diffraction pattern (the sample is square-shaped, and thus the diffraction pattern is cross-shaped). In principle, the hyperuniform networks scattering function should decay to zero asymptotically for $\theta \rightarrow 0$, with $q_\theta = (4\pi n/\lambda) \sin \theta/2 \rightarrow 0$. However, due to the overwhelming stray light and diffraction, we still observe a substantial increase in the scattering signal at small angles.

Despite the experimental difficulties, we can identify the peak of the scattering function, a signature of short-range order. For the original form we find a scattering maximum at $q_{\text{max}} = 4.5 \mu\text{m}^{-1}$ ($\theta_{\text{max}} = 17.4^\circ$) (Figure 2c). As discussed in earlier work^[22] the corresponding peak of the density auto-correlation function is given by the relation $q_{\text{max}} a/2\pi \approx 1.2$ and thus $a \approx 1.7 \mu\text{m}$, as expected. Previously the highest resolved network printed by DLW was based on jammed hard spheres as a seed pattern,^[19] with a diameter $2R_{\text{HS}} = 1.54 \mu\text{m}$ and

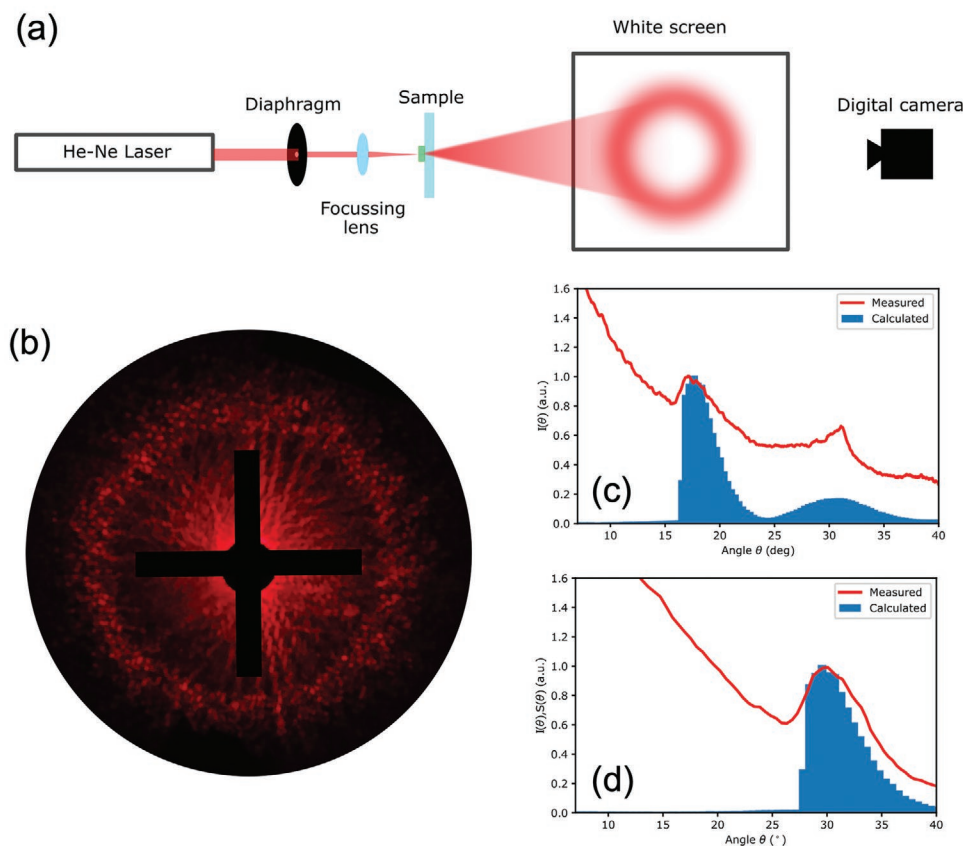


Figure 2. a) Schematic of the small-angle scattering setup. The red laser beam ($\lambda = 632.8$ nm) passes a diaphragm and is then focused on the sample. The scattered light is collected on a white screen, where an image is taken from the backside. Panel (b) shows a typical image taken with a digital camera. Some but not all of the stray lights can be masked (cross-shape). c) Radially averaged scattering intensity was recorded for the original polymer template and shrunken form (d), solid lines. Numerically we obtain the scattering function in the first Born (Rayleigh–Gans–Debye) scattering approximation by taking a Fourier transform of the discrete digital representation of the network. The blue shaded area shows the calculated scattering profiles.

$a = 2R_{\text{HS}}/0.935 = 1.65$.^[22,23] Here we use nearly identical settings for DLW. After shrinking the sample, the peak shifts to $7.6 \mu\text{m}^{-1}$ ($\theta_{\text{max}} = 29.5^\circ$) which corresponds to $a \approx 1 \mu\text{m}$, that is a size reduction by a factor 0.6 (Figure 2d).

We compare the experimental data with numerical predictions computing the Fourier transform of the original digital representation of the network $I(q_\theta)$. We convert the momentum transfer $q_\theta = |\vec{q}_\theta|$ to the scattering angle using $q_\theta = 4\pi n/\lambda \sin \theta/2$ with $n \approx 1.5$. For a comparison between numerical calculations of $I(q_\theta)$ and the shrunken forms, we uniformly rescale all length scales in the numerical calculations. We find qualitative agreement between experiments and numerical predictions around the peak and for larger angles as shown in Figure 2c,d.

2.3. Photonic Bandgap in Titania and Silicon Infiltrated Structures

Photonic features such as bandgaps require a substantial refractive index mismatch, and thus only infiltrating the structure with titania (TiO_2) or silicon, **Figure 3**, leads to prominent spectral features. Titania's refractive index is ≈ 2.4 and the index of amorphous silicon is ≈ 3.5 at $\lambda \approx 1.5 \mu\text{m}$ ^[40,41] compared to the polymer with about 1.5.^[42]

We increase the refractive index of the polymer network by depositing high index titania (TiO_2 , $n \approx 2.4$) via atomic layer deposition (ALD) and silicon (Si, $n \approx 3.5$) via chemical vapor deposition (CVD; see Experimental Section). 55 nm of TiO_2 was deposited via moderate temperature ALD ($T = 120$ °C) and up to about 100 nm of Si at $T = 480$ °C. For the latter, we first deposit ≈ 15 nm of TiO_2 to stabilize the polymer network. The polymer later becomes decomposed during the silicon CVD at 480 °C; see also Supporting Information in ref. [39].

We use a Fourier transform infrared spectrometer coupled to a microscope (Hyperion 2000, Bruker, Germany) to determine the sample's transmittance $T(\lambda)$. Transmitted light is collected over a finite acceptance angle $\approx 15^\circ$ (for details, see refs. [19,39,43]). We focus the incident light on a spot in the center of the sample (about $20 \times 20 \mu\text{m}^2$) and average over 200 measurements. As a reference for the transmittance, we measure the transmission spectrum on the substrate directly beside the sample. For all transmission measurements, the sample is held in air $n = 1$. In **Figure 4**, we plot the transmittance spectra for different amounts of titania added via ALD. We observe a shallow minimum after 700 ALD cycles of titania deposition, corresponding to a coating layer thickness of about 35 nm. With increasing titania filling fraction, we see a shift in the wavelength of the local minimum from 1.5 to 1.8 μm due

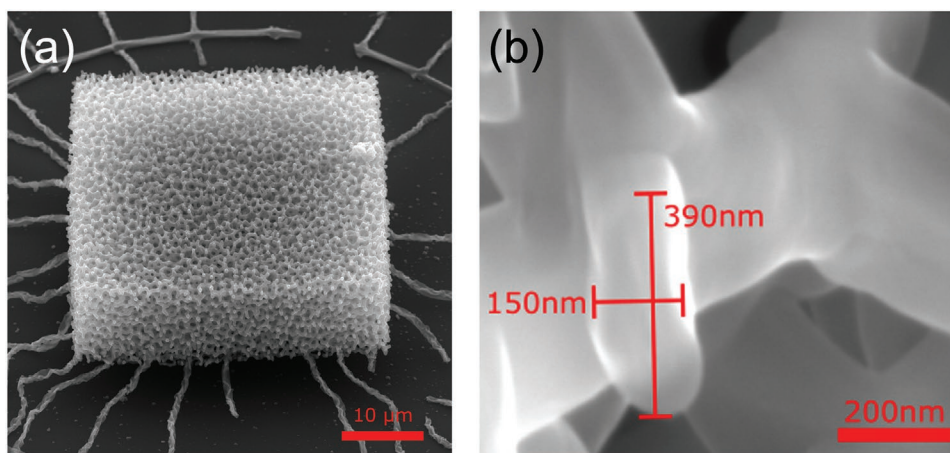


Figure 3. Scanning electron microscopy (SEM) and focused ion beam milling (FIB) of silicon networks. a) Titania stabilized and silicon infiltrated network, see also ref. [39]. The network structure and the overall shape of structure has been preserved throughout the different processing steps. Sample height: 12.3 μm, edge length, 38.2 μm. b) Cross section of a silicon infiltrated HU-network structure. A section of the structure was cut out using focused ion beam milling. The image is taken at an angle of 52°.

to the increase of the material's effective refractive index n_{eff} . At the same time, the minimum depth changes only slightly. The titania coating procedure has limitations due to the moderate titania refractive index. The polymer scaffold remains intact during the ALD titania deposition at only 120 °C leading to a high space filling fraction (polymer and titania combined).

Next, we proceed to silicon (Si) infiltration. Here we expect a more pronounced bandgap due to silicon's much higher refractive index, $n \approx 3.5$. However, since the CVD process operates at elevated temperatures, where polymer decomposes, we must first coat the scaffold with a thin but mechanically stable protective layer. To this end, we first deposit 300 ALD-cycles (≈ 15 nm) of titania on the polymer scaffold. During the heating and subsequent CVD, the polymer is decomposed (calcinated), and

the titania coated struts fully or partially collapse, resulting in thinner or composite Si/TiO₂ rods.^[39]

Using CVD, we deposit amorphous silicon; we start with a 4 min infiltration and then progressively add more Si in 2 min steps. The corresponding transmittance spectra are shown in Figure 4c,d. The dip indicating a PBG is much more pronounced for the Si-coated structures, and we indeed can report a clear photonic bandgap for $\lambda \approx 1.6$ μm in 3D hyperuniform networks at telecom wavelengths (1.3 μm < λ < 1.6 μm). In an earlier study,^[39] we observed that the titania shell collapses first, and the silicon deposition proceeds on the surface of thin titania rods. However, depending on the stability of the titania shell, this might not always be the case. We do not control the simultaneous calcination, titania shell collapse, and Si-coating

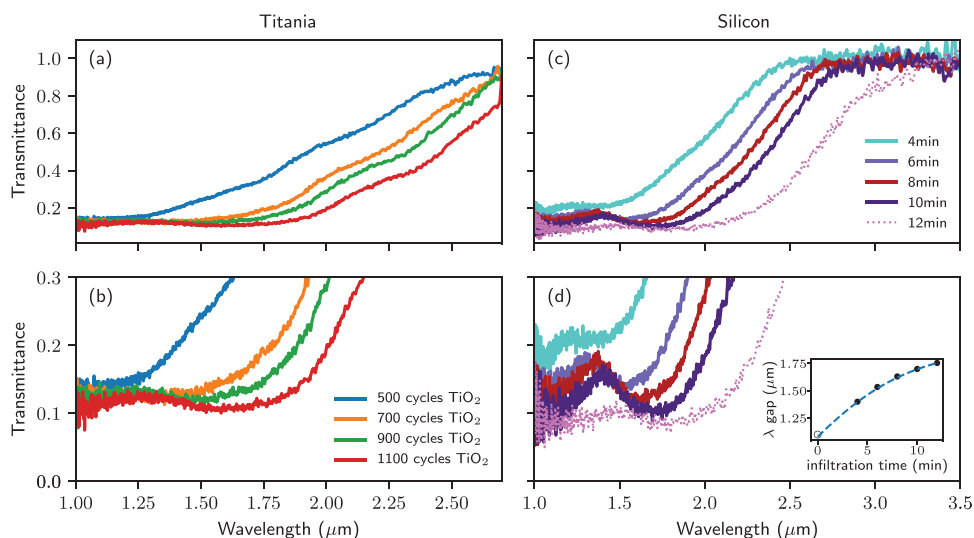


Figure 4. a,b) Transmittance spectra of titania infiltrated stealthy hyperuniform structure. The curves depict spectra for different amounts of added titania. The lower panel (b) shows an enlarged view of the spectra to resolve the features near the gap wavelength λ_{Gap} . c,d) Transmittance spectra of silicon infiltrated stealthy hyperuniform structure. The curves are normalized to one over $\lambda/\mu\text{m} \in [3.25, 3.5]$ by multiplication with a factor 1.2–1.4. The colors mark different infiltration times or different amounts of deposited silicon. The inset in (d) displays the shift of the gap center as the volume filling fraction increases. The dashed line is a guide to the eye.

process. However, we also do not expect significant differences in the photonic properties depending on the exact distribution of the residual titania in the final composite material. After shrinking, the pure polymer structure has a filling fraction of about 10%. The stabilizing titania layer increases the volume filling by about 2%, calculated using the procedure described in ref. [43]. Depositing amorphous silicon replaces the polymer and then increases the total volume filling up to 15–35%,^[39] depending on the silicon infiltration duration, see Figure 3b and inset of Figure 4d.

3. Discussion and Conclusions

This work implemented thermal processing for DLW fabricated hyperuniform networks to shrink them uniformly. Using small-angle scattering from nearly refractive index-matched samples, we could show that the polymer networks remain intact during shrinkage. To this end, we find that short-range structural correlations scale with reducing the overall sample size. We achieve an almost twofold gain of fabrication resolution for photonic structures bringing spectral features, such as band gaps, in the near-infrared spectral range. Combined with enhanced STED-inspired DLW, one could even target visible wavelengths in the future.

The smallest center gap position reported so far was $\lambda_{\text{Gap}} \approx 2.4 \mu\text{m}$.^[19] After infiltrating the structures with high index silicon, our measurements reveal a gap center wavelength between $\lambda_{\text{Gap}} = 1.5 \mu\text{m}$ and $\lambda_{\text{Gap}} = 1.7 \mu\text{m}$, substantially lower than in previous studies on hyperuniform dielectric networks in 3D. Based on this study's significant progress, we can now consider fabricating structures of sufficient height to study bulk behavior, showing transmission attenuation inside the gap and substantial multiple light scattering elsewhere. In addition, recent numerical simulations suggest that measurements of transport properties open realistic pathways to detect Anderson localization and distinguish it from transport in a PBG.^[23,44]

With heat-induced shrinkage, we can expand the toolbox of spectrally resolved measurement techniques using standard equipment, such as supercontinuum lasers and digital cameras, whose availability and performance are limited for larger wavelengths. A bandgap at wavelengths smaller than $\lambda_{\text{Gap}} = 1.7 \mu\text{m}$ makes it possible to characterize the structures using standard digital cameras and single-photon detectors, for example, for measuring speckle or time-resolved transmission.^[30,45] In the latter case, measurements are sensitive to the photonic material's transmission channels, which one can now probe in the NIR by studying speckle fluctuations' space and frequency dependence. In conclusion, the progress reported in this work opens up many exciting possibilities for the design and study of such novel disordered photonic materials.

4. Experimental Section

Structural Design: To generate a hyperuniform network with tetrahedral coordination, a stealthy hyperuniform (SHU) seed point pattern, $\chi = 0.65$, containing $N = 10\,000$ points in a cubic box (with periodic boundary conditions) following a generalization to three dimensions of the algorithm presented in ref. [24] was created. To avoid any finite-size

effects in the following processing, the original point pattern was replicated⁴ in the three directions, creating an extended pattern with 3^3N points. A Delaunay (tetrahedral) tessellation was performed on the extended seed point pattern using the Delaunay function of the Python Scipy.spatial library.^[46] The center of mass of each tetrahedron was linked to the respective centers of the neighboring tetrahedra. All line segments lying outside of the original box were removed. Hence, any finite size effect associated with the tessellation next to the boundary of the extended pattern was removed. This procedure defined a fourfold connected network of rods with $\mathcal{O}N^{3/2}$ nodes; in this case, the number of nodes was $\approx 1.7 \times 10^6$. The network was coded for DLW using the NanoScribe proprietary software package called DeScribe^[35] such that the first peak of the angle-averaged density autocorrelation function was located at $a = 1.75 \mu\text{m}$.^[22]

Direct Laser Writing: The commercially available DLW instrument Photonic professional GT+ (Nanoscribe GmbH, Germany) was used. The instrument's light source was a femtosecond pulsed laser with a wavelength of 780 nm. In addition, an acoustic-optical modulator to adjust the laser power was used. This was operated in stage scanning mode and the most petite feature sizes were achieved using Zeiss's 1.4 NA 63 \times oil immersion objective illuminating the sample from below. The scanning stage consisted of two units, a piezo scanning stage with a nanometer positional accuracy and a maximum scanning volume of $300 \times 300 \times 300 \mu\text{m}^3$, and a motorized mechanical translation stage. The microscope z-drive could move the sample up and down on the vertical axis without practical limitations. The writing speeds were typically tenths of micrometers per second for the piezo stage. The writing process was monitored using a charged-coupled device camera coupled to a port at the bottom part of the microscope. In addition, a beamsplitter underneath the objective allowed for the observation of the writing process.

The dip-in configuration was used to immerse the objective directly in the viscous resin and start writing the structures from the top (upside down). There were no glass plates or other interfaces between the microscope objective and the exposed voxel. Also, the laser did not have to pass through the exposed resin. The object's height was only limited by the amount of resin between the objective and the substrate.

Choosing the suitable resin is of utmost importance. It can impact essential characteristics such as the feature size, absorption, the refractive index, and roughness, to mention a few. The resist used here was the negative-tone photoresist developed by Nanoscribe, IP-Dip, which does not require pre- or post-baking. It shows limited memory effects, meaning that underexposed resin does not readily polymerize when exposed multiple times to intensities lower than the threshold. The voxel could be as small as $\approx 150 \text{ nm}$ in the lateral direction with an aspect ratio of ≈ 2.7 .^[47]

A developer solution (propylene glycol monomethyl ether acetate (PGMEA)) was used to dissolve non-exposed resist. To this end, the samples were immersed twice in a PGMEA bath. Next, the sample was washed in a low surface tension liquid, isopropanol, and dried in the CPD.

Critical Point Drying: Despite using a low surface tension fluid, capillary forces stress the structure. Especially for high-resolution network structures, these forces damage the sample. CPD is the best method to avoid deformation altogether. It allows bypassing the liquid–gas transition, thereby avoiding any capillary forces. The CPD (Leica EM CPD 300) exchanged isopropanol with carbon dioxide in several cycles at about 50 bar. The carbon dioxide was heated to 35 °C while the pressure rose to 75 bar to get around the critical point. Under these conditions, carbon dioxide remains supercritical. Next, the pressure was released to return the carbon dioxide to its gaseous state.

Titania Infiltration: The shrunken structures were post processed via the deposition of titania (TiO_2) using ALD.^[48] The moderate-temperature ALD-step also allowed the stabilization of the polymer network before starting the high-temperature deposition of silicon described later in the text. ALD is a self-limiting gas–solid reaction-based deposition technique capable of covering complex systems with inorganic compounds at a thickness down to the nanometer range. ALD has

become of interest for high-index photonic structures as it opens the possibility for the fabrication of high-index nano- and microstructures. The principle of the ALD process is to expose the sample's surface alternatively to different precursors for a layer-by-layer deposition of the desired compound material. Precursors are separated in the gas phase in contrast to CVD, as discussed later in the text. Here a commercially available ALD reactor (Savannah 100, Cambridge Nanotech Inc., MA, USA) was used. The ALD reactor was operated at 120 °C and titania was deposited at a growth rate of around 0.5 Å per cycle.

Chemical Vapor Deposition: Silicon is one of the most popular choices for designing photonic bandgap materials.^[14,49] It has a high refractive index of $n \approx 3.5$ at telecom wavelengths around $\lambda \approx 1.5 \mu\text{m}$ ^[47] and shows negligible absorption for wavelengths above 1.1 μm . CVD is an established method of depositing silicon on polymeric templates.^[6] However, due to the high activation temperature of the CVD process, it was not possible to deposit silicon directly on the polymer structure. On the other hand, titania-coated systems provided a satisfactory stable skeleton for silicon infiltration.^[39] The CVD process relies on the decomposition of a precursor in the gas phase at the sample's surface.^[6] In contrast to ALD, CVD operates with a constant gas flow. As a result, the deposition itself is not a layer-by-layer process but proceeded continuously. The resulting silicon coating is amorphous or polycrystalline. With several nanometers per minute, the CVD process is faster than ALD. As the characterization will be done in transmission, a second glass slide was first glued using a silver paste on the backside of the substrate to avoid deposition of silicon. Next, the sample was loaded into the CVD reactor with the sample pointing upward. The chamber was evacuated and a little nitrogen flow was leaked to avoid oxygen contamination in the reactor and dilute the precursor gas. The pressure was held at about 7 mbar while the chamber was heated to around 480 °C over ≈ 20 min. As a precursor disilane (Si_2H_6) gas was used. At about 300 °C, the decomposition into silane (SiH_4) and silylene (SiH_2) starts. Finally, the reactants transformed further to silicon at 480 °C. The flow of the disilane precursor was set to 3 $\text{cm}^3 \text{ s}^{-1}$. In parallel, at 480 °C, the polymer scaffold is thermally decomposed; see Supporting Information in ref. [39]. Images of titania stabilized, and silicon infiltrated network are shown in Figure 3.

Scattering Properties of the Polymer Template: The light scattering properties of the structure are modeled in the first Born or Rayleigh–Gans–Debye (RGD) approximation assuming scattering from independent dipole volume elements.^[50] To this end, the volume rendering of the system was discretized in a sufficiently densely spaced binary matrix and a 3D fast Fourier transformation was performed. Here n is defined as the number of volume pixels (voxels) in 1D, $N = n^3$ is the total number of voxels. The origin will be at the corner of the matrix, so the origin was shifted to the center of the matrix for a more straightforward representation. The structure factor is then given by

$$S(\vec{k}) = \frac{1}{N} \sum_{i,j=0}^N \rho(\vec{r}_i) \rho(\vec{r}_j) e^{i\vec{k} \cdot (\vec{r}_i - \vec{r}_j)} = \frac{1}{N} |\text{FFT}|^2 \quad (1)$$

with $r_{i,j}$ being the position of the scatterers.

From this, the differential cross-section $\frac{d\sigma_{\text{scatt}}}{d\Omega}$ could be calculated, see histogram in Figure 2c,d. In the RGD approximation, where every voxel is considered as a single scatterer, and averaged over all polarizations, the differential cross-section can be written as

$$\frac{d\sigma_{\text{scatt}}}{d\Omega} = \frac{1}{k^2} |\alpha|^2 \sum_{n,m} e^{i\vec{q} \cdot (\vec{r}_n - \vec{r}_m)} \left[1 - \frac{1}{2} \sin^2 \theta \right] \quad (2)$$

with

$$\alpha = \frac{3}{4\pi} (k\Delta x)^3 \frac{\epsilon_n - \epsilon_h}{\epsilon_n + 2\epsilon_h} \quad (3)$$

being the dimensionless polarizability of the voxel with side length Δx . k is the wave number, ϵ_n is the permittivity of the “occupied” voxel, and ϵ_h the one of the host medium. The momentum transfer or scattering vector is defined as $\vec{q} \equiv \vec{k}_{\text{in}} - \vec{k}_{\text{scatt}}$.

Since the differential scattering cross-section does not depend on the ϕ angle, it can be written as

$$\begin{aligned} \frac{d\sigma_{\text{scatt}}(\theta)}{d\theta} &= \frac{\pi}{k^2} |\alpha|^2 \sin \theta (1 + \cos^2 \theta) \sum_{n,m} e^{i\vec{q} \cdot (\vec{r}_n - \vec{r}_m)} \\ &= \frac{\pi}{k^2} |\alpha|^2 \sin \theta (1 + \cos^2 \theta) \times N \times S(\vec{q}). \end{aligned} \quad (4)$$

Acknowledgements

The authors thank Michael Engel for sharing the original 3D code to generate the stealthy hyperuniform point pattern. The Swiss National Science Foundation financially supported this work through the National Center of Competence in Research Bio-Inspired Materials, No. 182881, and through projects No. 169074, No. 197146, and No. 188494.

Open access funding provided by Universite de Fribourg.

Conflict of Interest

The authors declare no conflict of interest.

Data Availability Statement

The data that support the findings of this study are openly available in zenodo at <https://doi.org/10.5281/zenodo.5931238>, reference number 5931238.

Keywords

amorphous dielectric networks, bandgap, direct laser writing, hyperuniformity, nanofabrication

Received: January 31, 2022

Revised: May 23, 2022

Published online:

- [1] K. M. Ho, C. T. Chan, C. M. Soukoulis, R. Biswas, M. Sigalas, *Solid State Commun.* **1994**, *89*, 413.
- [2] K. Edagawa, S. Kanoko, M. Notomi, *Phys. Rev. Lett.* **2008**, *100*, 013901.
- [3] S. R. Sellers, W. Man, S. Sahba, M. Florescu, *Nat. Commun.* **2017**, *8*, 14439.
- [4] M. He, J. P. Gales, E. Ducrot, Z. Gong, G.-R. Yi, S. Sacanna, D. J. Pine, *Nature* **2020**, *585*, 524.
- [5] M. A. Klatt, P. J. Steinhardt, S. Torquato, *Proc. Natl. Acad. Sci. USA* **2019**, *116*, 23480.
- [6] J. Ricouvier, R. Pierrat, R. Carminati, P. Tabelaing, P. Yazhgur, *Phys. Rev. Lett.* **2017**, *119*, 208001.
- [7] L. S. Froufe-Pérez, M. Engel, P. F. Damasceno, N. Muller, J. Haberko, S. C. Glotzer, F. Scheffold, *Phys. Rev. Lett.* **2016**, *117*, 053902.
- [8] W. Man, M. Florescu, E. P. Williamson, Y. He, S. R. Hashemizad, B. Y. Leung, D. R. Liner, S. Torquato, P. M. Chaikin, P. J. Steinhardt, *Proc. Natl. Acad. Sci. USA* **2013**, *110*, 15886.
- [9] M. M. Milošević, W. Man, G. Nahal, P. J. Steinhardt, S. Torquato, P. M. Chaikin, T. Amoah, B. Yu, R. A. Mullen, M. Florescu, *Sci. Rep.* **2019**, *9*, 20338.

- [10] N. Granchi, R. Spalding, M. Lodde, M. Petruzzella, F. W. Otten, A. Fiore, F. Intonti, R. Sapienza, M. Florescu, M. Gurioli, *Adv. Opt. Mater.* **2022**, *10*, 2102565.
- [11] V. Hwang, A. B. Stephenson, S. Magkiriadou, J.-G. Park, V. N. Manoharan, *Phys. Rev. E* **2020**, *101*, 012614.
- [12] S. Kinoshita, S. Yoshioka, J. Miyazaki, *Rep. Prog. Phys.* **2008**, *71*, 076401.
- [13] L. Schertel, L. Siedentop, J.-M. Meijer, P. Keim, C. M. Aegerter, G. J. Aubry, G. Maret, *Adv. Opt. Mater.* **2019**, *7*, 1900442.
- [14] A. Blanco, E. Chomski, S. Grabtchak, M. Ibsate, S. John, S. W. Leonard, C. Lopez, F. Meseguer, H. Miguez, J. P. Mondia, G. A. Ozin, O. Toader, H. M. van Driel, *Nature* **2000**, *405*, 437.
- [15] M. Deubel, G. Von Freymann, M. Wegener, S. Pereira, K. Busch, C. M. Soukoulis, *Nat. Mater.* **2004**, *3*, 444.
- [16] N. Tétreault, G. von Freymann, M. Deubel, M. Hermatschweiler, F. Pérez-Willard, S. John, M. Wegener, G. A. Ozin, *Adv. Mater.* **2006**, *18*, 457.
- [17] I. Staude, M. Thiel, S. Essig, C. Wolff, K. Busch, G. von Freymann, M. Wegener, *Opt. Lett.* **2010**, *35*, 1094.
- [18] C. Marichy, N. Muller, L. S. Froufe-Pérez, F. Scheffold, *Sci. Rep.* **2016**, *6*, 21818.
- [19] N. Muller, J. Haberko, C. Marichy, F. Scheffold, *Optica* **2017**, *4*, 361.
- [20] M. Florescu, S. Torquato, P. J. Steinhardt, *Proc. Natl. Acad. Sci. USA* **2009**, *106*, 20658.
- [21] G. J. Aubry, L. S. Froufe-Pérez, U. Kuhl, O. Legrand, F. Scheffold, F. Mortessagne, *Phys. Rev. Lett.* **2020**, *125*, 127402.
- [22] S. F. Liew, J.-K. Yang, H. Noh, C. F. Schreck, E. R. Dufresne, C. S. O'Hern, H. Cao, *Phys. Rev. A* **2011**, *84*, 063818.
- [23] J. Haberko, L. S. Froufe-Pérez, F. Scheffold, *Nat. Commun.* **2020**, *11*, 4867.
- [24] L. S. Froufe-Pérez, M. Engel, P. F. Damasceno, N. Muller, J. Haberko, S. C. Glotzer, F. Scheffold, *Phys. Rev. Lett.* **2016**, *117*, 053902.
- [25] E. Abrahams, *50 Years of Anderson Localization*, Vol. 24, World Scientific, Singapore **2010**.
- [26] L. S. Froufe-Pérez, M. Engel, J. J. Sáenz, F. Scheffold, *Proc. Natl. Acad. Sci. USA* **2017**, *114*, 9570.
- [27] S. Torquato, *Phys. Rep.* **2018**, *745*, 1.
- [28] R. D. Batten, F. H. Stillinger, S. Torquato, *J. Appl. Phys.* **2008**, *104*, 033504.
- [29] Q. Wang, S. Stobbe, P. Lodahl, *Phys. Rev. Lett.* **2011**, *107*, 167404.
- [30] T. Strudley, T. Zehender, C. Blejean, E. P. Bakkers, O. L. Muskens, *Nat. Photonics* **2013**, *7*, 413.
- [31] G. Aubry, N. Fuchs, S. Skipetrov, F. Scheffold, *Opt. Lett.* **2022**, *47*, 1439.
- [32] P. Kaplan, A. Dinsmore, A. Yodh, D. Pine, *Phys. Rev. E* **1994**, *50*, 4827.
- [33] J. Fischer, G. von Freymann, M. Wegener, *Adv. Mater.* **2010**, *22*, 3578.
- [34] Y. Liu, H. Wang, J. Ho, R. C. Ng, R. J. H. Ng, V. H. Hall-Chen, E. H. H. Koay, Z. Dong, H. Liu, C.-W. Qiu, J. R. Greer, J. K. W. Yang, *Nat. Commun.* **2019**, *10*, 3578.
- [35] J. Haberko, F. Scheffold, *Opt. Express* **2013**, *21*, 1057.
- [36] J. Haberko, N. Muller, F. Scheffold, *Phys. Rev. A* **2013**, *88*, 043822.
- [37] M. Renner, G. von Freymann, *Adv. Opt. Mater.* **2014**, *2*, 226.
- [38] G. Von Freymann, A. Ledermann, M. Thiel, I. Staude, S. Essig, K. Busch, M. Wegener, *Adv. Funct. Mater.* **2010**, *20*, 1038.
- [39] N. Muller, J. Haberko, C. Marichy, F. Scheffold, *Adv. Opt. Mater.* **2014**, *2*, 115.
- [40] M. Reufer, L. F. Rojas-Ochoa, S. Eiden, J. J. Sáenz, F. Scheffold, *Appl. Phys. Lett.* **2007**, *91*, 171904.
- [41] J. Kischkat, S. Peters, B. Gruska, M. Semtsiv, M. Chashnikova, M. Klinkmüller, O. Fedosenko, S. Machulik, A. Aleksandrova, G. Monastyrskyi, Y. Flores, W. T. Masselink, *Appl. Opt.* **2012**, *51*, 6789.
- [42] S. Dottermusch, D. Busko, M. Langenhorst, U. W. Paetzold, B. S. Richards, *Opt. Lett.* **2019**, *44*, 29.
- [43] S. Aeby, G. J. Aubry, N. Muller, F. Scheffold, *Adv. Opt. Mater.* **2021**, *9*, 2001699.
- [44] F. Scheffold, J. Haberko, L. S. Froufe-Pérez, *arXiv:2204.07774*, **2022**.
- [45] L. Rojas, M. Bina, G. Cerchiarì, M. Escobedo-Sanchez, F. Ferri, F. Scheffold, *Eur. Phys. J.: Spec. Top.* **2011**, *199*, 167.
- [46] P. Virtanen, R. Gommers, T. E. Oliphant, M. Haberland, T. Reddy, D. Cournapeau, E. Burovski, P. Peterson, W. Weckesser, J. Bright, S. J. van der Walt, M. Brett, J. Wilson, K. J. Millman, N. Mayorov, A. R. J. Nelson, E. Jones, R. Kern, E. Larson, C. J. Carey, Í. Polat, Y. Feng, E. W. Moore, J. VanderPlas, D. Laxalde, J. Perktold, R. Cimrman, I. Henriksen, E. A. Quintero, C. R. Harris, et al., *Nat. Methods* **2020**, *17*, 261.
- [47] M. Deubel, G. von Freymann, M. Wegener, S. Pereira, K. Busch, C. M. Soukoulis, *Nat. Mater.* **2004**, *3*, 444.
- [48] N. Pinna, M. Knez, *Atomic Layer Deposition of Nanostructured Materials*, John Wiley & Sons, Hoboken, NJ **2012**.
- [49] J. Joannopoulos, S. Johnson, J. Winn, R. Meade, *Photonic Crystals: Molding the Flow of Light*, 2nd ed., Princeton University Press, Princeton, NJ **2008**.
- [50] H. C. van de Hulst, *Light Scattering by Small Particles*, Dover Publications Inc, Mineola, NY **1981**.